



HyM3D: A hybrid method for the automatic 3D reconstruction of a defective cranial vault

Antonio Marzola^{a,*}, Kathleen S. McGreevy^b, Federico Mussa^b, Yary Volpe^a, Lapo Governi^a

^a Department of Industrial Engineering of Florence, University of Florence (Italy), via di Santa Marta 3, Firenze 50139, Italy

^b Meyer Children's Hospital IRCCS, Viale Pieraccini 24, Florence 50141, Italy

ARTICLE INFO

Article history:

Received 21 December 2022

Revised 8 March 2023

Accepted 27 March 2023

Keywords:

Computed aided design

Bioinformatics

Statistical shape model

Surface Interpolation

Cranioplasty

ABSTRACT

Background and objective: The ability to accomplish a consistent restoration of a missing or deformed anatomical area is a fundamental step for defining a custom implant, especially in the maxillofacial and cranial reconstruction where the aesthetical aspect is crucial for a successful surgical outcome. At the same time, this task is also the most difficult, time-consuming, and complicated across the whole reconstruction process. This is mostly due to the high geometric complexity of the anatomical structures, insufficient references, and significant interindividual anatomical heterogeneity. Numerous solutions, specifically for the neurocranium, have been put forward in the scientific literature to address the reconstruction issue, but none of them has yet been persuasive enough to guarantee an easily automatable approach with a consistent shape reconstruction.

Methods: This work aims to present a novel reconstruction method (named HyM3D) for the automatic restoration of the exocranial surface by ensuring both the symmetry of the resulting skull and the continuity between the reconstructive patch and the surrounding bone. To achieve this goal, the strengths of the Template-based methods are exploited to provide knowledge of the missing or deformed region and to guide a subsequent Surface Interpolation-based algorithm. HyM3D is an improved version of a methodology presented by the authors in a previous publication for the restoration of unilateral defects. Differently from the first version, the novel procedure applies to all kinds of cranial defects, whether they are unilateral or not.

Results: The presented method has been tested on several test cases, both synthetic and real, and the results show that it is reliable and trustworthy, providing a consistent outcome with no user intervention even when dealing with complex defects.

Conclusions: HyM3D method proved to be a valid alternative to the existing approaches for the digital reconstruction of a defective cranial vault; furthermore, with respect to the current alternatives, it demands less user interaction since the method is landmarks-independent and does not require any patch adaptation.

© 2023 Elsevier B.V. All rights reserved.

1. Introduction

Cranial defects are usually the result of trauma, tumor resections, congenital dysmorphisms, or complications of previous surgery. Patients with these defects suffer negative effects on a functional level (from headaches up to neurological impairment) as well as on an emotional and social sphere. In fact, by affecting the normal facial shape, it is well-recognized that defect-related consequences are connected to decreased social and emotional functioning [1]. Consequently, the success of a cranioplasty, i.e. the surgical procedure to repair a cranial hole, resides in restoring the full func-

tionality of the cranial vault as well as in recovering satisfactory aesthetics. When the original bone flap cannot be reimplanted, an allograft should be used to fill the gap. In this case, two approaches are possible: the first requires the intra-operative shaping of the reconstructive device, while the second uses a pre-operatively designed and fabricated device. Indeed, the best way to improve the aesthetic outcome is by using the second approach [2,3], since the first one totally relies on the surgeon's ability.

By considering the typical workflow followed in the pre-operative design and fabrication strategy schematically shown in Fig. 1, the reconstruction of the region of interest (ROI) results to be the most influencing for the achievement of a satisfying aesthetics outcome, since it provides the actual shape of the prosthesis. At the same time, this task is also the most difficult and

* Corresponding author.

E-mail address: antonio.marzola@unifi.it (A. Marzola).

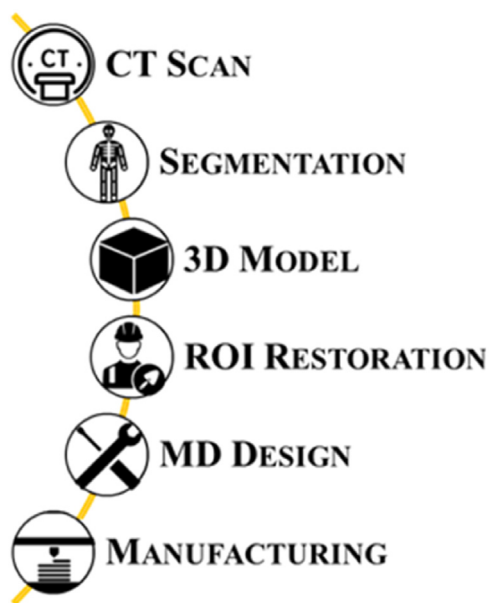


Fig. 1. Typical Medical Device (MD) CAx Framework.

time-consuming for the user: the ROI often has malformations or missing parts, and there is no information available to guide a consistent restoration, mainly due to the wide variability and high complexity of the human anatomy. The need of obtaining an accurate reconstruction and the complexity of the task has led to extensive literature published on the subject [4]. A thorough analysis of the State-of-the-Art (SoA) reveals a wide range of alternatives proposed to achieve a cranial vault reconstruction that is consistent and, at the same time, as fast to implement and as simple as possible. To ensure a consistent result, i.e. to provide a reliable reconstruction considering both functional and aesthetical aims, all the studies proposed in the literature deal with how to find the missing information to achieve a restored skull as symmetrical as possible and how to ensure the continuity between the reconstructed patch and the surrounding healthy bone.

Furthermore, there is a great interest in automating the framework presented in Fig. 1 in order to speed it up, because the time between the diagnosis and the surgical intervention can be critical in some applications (as in oncology). This goal can be obtained by making the instruments available also to less experienced CAx users or directly to surgeons, and eliminating all time-consuming, repetitive, and lengthy user operations. Moreover, by using an automatic procedure, it is possible to standardize and maximize the repeatability of the whole design process. Nowadays, SoA techniques can be grouped into four different reconstructive approaches, depending on the strategy used for the reconstruction: (i) the *Template-based approach* uses prior knowledge provided by an external source which contains information on the expected full shape, enabling a data-guided reconstruction of the cranial bones; (ii) the *Surface Interpolation-based approach* uses a mathematical surface that interpolates the edge of the defect; (iii) the *Slice-based approach* deforms a mathematical curve to wrap the contour of the healthy bone slice-by-slice; (iv) the *Machine Learning-based approach*, to automatically infer the restored shape using deep learning techniques applied to an adequate number of Computed Tomography (CT) scans of healthy human skulls.

A comprehensive description of the most representative methods based on the first three approaches mentioned above, with their strengths and limitations, is presented in [4]. Regarding the *machine learning-based approach*, not covered by [4], to date there are no reliable methods that actually work on real bone geometries

because the 3D model to be analyzed is usually deformed or injured and significantly differs from the healthy ones used for the training process.

In summary, the SoA analysis shows that, up to date, a convincing solution has not been yet proposed: all existing approaches have weaknesses and limitations, which often consist of either a high user interaction request or a lack of a-priori available data. These issues usually prevent the achievement of an aesthetically acceptable reconstruction, especially in case of wide defects. To overcome these drawbacks, in a previous research [5] the authors proposed a new *hybrid* procedure for the semi-automatic restoration of the outer surface of a defective or deformed neurocranium. The proposed method proved to be able to ensure an adequate symmetry of the resulting skull and the continuity between the bone and the reconstructive patch. The approach was named *hybrid* since a *Surface Interpolation-based approach* is used for actually filling the hole but, to ensure a consistent reconstruction, the interpolation is driven by a template able to compensate for the lack of information in the deformed or missing areas. The template used in [5] was the healthy half of the skull under consideration, which was mirrored around the mid-sagittal plane (automatically retrieved by means of the procedure described in [6]) and then registered onto the contralateral half. Clearly, the algorithm proposed in [5] has a significant limitation: being a mirroring & registration-based approach is not applicable in situations where the contralateral side cannot be used as the reconstruction template (e.g., whenever the symmetrical counterpart does not exist, is deformed or even missing). As a consequence, it is suitable just for the restoration of unilateral defects.

In this work, the applicability of the original *hybrid* approach is expanded to include any kind of defect, unilateral and non-unilateral, by considering a Statistical Shape Model (SSM) of the neurocranium as a template during the restoration process. SSM is a parametric model able to infer the most likely full shape starting from its partial knowledge. The SSM used in this paper has been built according to a procedure developed by the authors and presented in [7]. The improved method is called “HyM3D” (Hybrid Method for 3D reconstruction of defective skulls).

In the following, “*Methods and Tools*” section provides a comprehensive description of the new procedure, while in “*Results*” section some test cases, which have been addressed to prove the robustness of the improved method, are presented together with the tests performed to tune the inputs of the algorithm.

2. Methods and tools

2.1. Data representation

A discrete description based on a set of points distributed throughout the surface, commonly referred to as “landmarks”, is the simplest but also the most general method for describing complex shapes [8,9]. The resulting discrete model is called Point Distribution Model (PDM) [10]. In early approaches, *landmarks* refer to salient feature points and are usually manually selected. To date, a dense set of points is used to deliver an adequate representation of complex 3D models. Therefore, landmarks are not located as per the common definition (i.e., they do not indicate only salient features) but are extracted from the whole volumetric model by proper algorithms. In medical applications, the volume data representing the ROI is obtained through a segmentation task performed on the diagnostic images by using dedicated software packages. From such volumetric data, a set of points are then sampled from the external surface of the shape, usually by using the Marching Cube algorithm. The result is a matrix (henceforward named Γ) that contains the 3D coordinates of each point. The matrix Γ de-

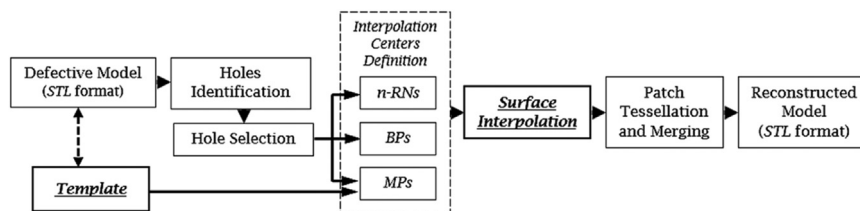


Fig. 2. The HyM3D method workflow.

scribes the 3D shape as PDM:

$$\Gamma = \{ \mathbf{x}_k | \mathbf{x}_k \in \mathbb{R}^3, k = 1, \dots, N \} \quad (1)$$

In Eq. (1), N represents the number of points used to describe the shape, and \mathbf{x}_k is the vector containing the 3D coordinates of each point of the PDM usually provided in a well-defined Cartesian coordinate frame x , y , and z :

$$\mathbf{x}_k = (x_k, y_k, z_k) \quad (2)$$

In addition to the PDM, from the volume data it is possible to retrieve also the connectivity information between the points \mathbf{x}_k . This information allows the calculation of the normal vectors all along the shape and, therefore, the reconstruction of its external surface. A point set with a connectivity list is called a *mesh*, and it is usually saved in STL format. Commercial software systems (e.g., Materialise Mimics® or 3DSlicer®) automatically perform the whole process from the segmented images to the STL file.

PDMs or STLs are widely used for the study of biological shapes [8,11] because, although their representation is discrete and the information they contain is low-level, this approach allows complex geometries (including those usually depicting anatomical structures) to be encoded in a mathematically valid and compact manner.

The restoring method proposed in this work requires the 3D model of the ROI to be provided as an STL file. Consequently, all mathematical definitions will be referred to a 3D model in the form of an STL file, i.e. described by a set of points \mathbf{x}_k and the related connectivity list.

2.2. The HyM3D method

The HyM3D method is an automatic algorithm to restore the full shape of a defective human cranial vault. As reported in the *Introduction*, it is an improvement of the *hybrid* approach for the restoration of unilateral cranial defect proposed by the authors in [5]. With respect to the original algorithm, HyM3D is able to face any kind of cranial defects, whether they are unilateral or not. HyM3D shares the same steps as well as the same concepts and mathematical formulation with the original method except for the introduction of an external source to serve as a template during the reconstruction process. The external source is meant to replace the contralateral half of the skull used in the original approach.

HyM3D represents a novel reconstruction method to address the issues identified by the SoA analysis and discussed in the *Introduction*. In fact, it aims to allow the automatic restoration of the exocranial surface, ensuring both the symmetry of the resulting skull and the continuity between the reconstructive patch and the surrounding bone. This aim is accomplished by exploiting the strengths of the existing approaches to overcome their limitations. A *Surface Interpolation-based* approach has the great advantage of allowing an easy automatization of the full process as well as imposing mathematically the continuity at the edge of the defect, but it usually leads to non-consistent results for large holes [12] due to the lack of information within the defective region. On the contrary, a *Template-based* approach is able to provide the missing information (within the defective region), but requires high user in-

teraction to obtain a good matching between the deformed template and the model to be reconstructed; moreover, also in case of an excellent matching, post-processing is still required to ensure continuity between the reconstructive patch and the healthy bone. As stated in the *Introduction*, the *hybrid* approach exploits the ability of the *Template-based* methods to provide knowledge of the missing or deformed region to guide a *Surface Interpolation-based* algorithm. Adding meaningful information within the affected region allows an easily automatable data-driven consistent reconstruction. The *hybrid* approach is then characterized by a user interaction limited to the preparation of the initial model and to the selection of the hole to be restored: this results in a less cumbersome and less time-consuming procedure when compared with both *Template-based* or *Slice-based* approaches. The whole reconstructive procedure is summarized in Fig. 2.

The first step is the automatic detection of all holes in the defective external surface of the cranial vault (see [5] for additional details on this step). Among the identified holes, the user is asked to manually select a point on the edge of the hole that must be restored (the algorithm restores a hole at a time); this operation represents the only interaction required to the user and it is necessary to avoid the algorithm to close all the gaps in the model. In fact, there are gaps that must not be restored, such as the external acoustic meatus, the orbits, and the underside of the skull. After that, the algorithm automatically finds the interpolation centers for the subsequent surface interpolation. Such centers are the points located at the boundary of the defect, named Boundary Points (BPs), and some additional points within the hole which are retrieved from the external source. The points within the defect, named Missing Points (MPs), are extracted from the template model after fitting the SSM onto the defective one; the eligible MPs are all the template's points located within the boundary loop of the defect to be restored. To avoid any discontinuity at the edge, only the innermost points (with respect to the hole to be filled) are considered MPs. In particular, only the eligible points that have a distance at least equal to m from the boundary loop are effectively kept as MPs, where m is an input to the algorithm. The greater is m the smaller the area of the hole covered by the MPs.

Additional points of the defective cranial vault lying on the outer side of the boundary loop and within a given distance n from the edge, named n -Ring Neighbors (n -RNs), are also taken into consideration as interpolation centers in addition to MPs and BPs. n -RNs allow to create an overlapping region between the reconstructed surface and the healthy skull to ensure the continuity between the healthy bone and the corrective patch. n is an input to the algorithm and the greater is n , the wider the overlapped region.

Fig. 3 provides a visual explanation of all the interpolation centers.

The actual interpolation is performed by using a Radial Basis Function (RBF) named Thin Plate Spline (TPS). It proved to be the most suitable in this application since it ensures a C^1 continuity, provides the smoothest result, and guarantees the lowest computational burden [13]. Furthermore, RBF imposes few restrictions on the nodes' geometry and can be used on scattered data with large data-free regions.

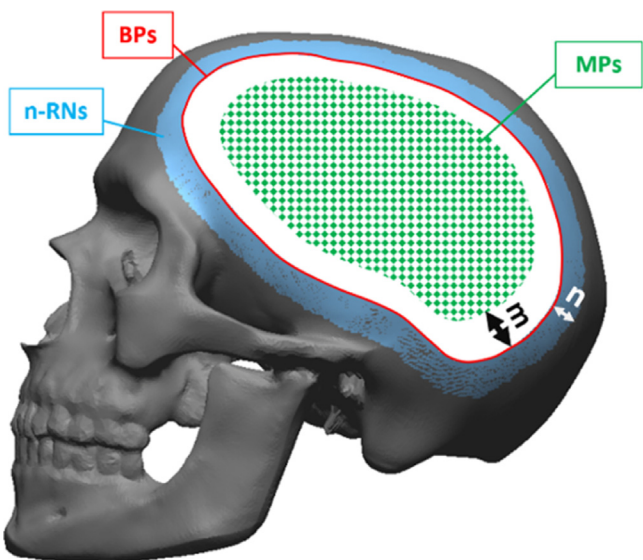


Fig. 3. Interpolation centers.

It is worth mentioning that, by using TPS, the interpolation condition is avoided in favor of an approximation of the centers: this brings many advantages in terms of computation time and smoothness, but an iterative refinement on the BPs is required to ensure an adequate continuity between the bone and the patch.

The resulting surface is then cut with the boundary loop and merged with the initial neurocranium to obtain the restored anatomy.

A comprehensive description of each step as well as the full mathematical formulation of the described method can be found in [5].

2.3. The statistical shape model in HyM3D

As stated in the *Introduction*, to allow the improved version of the *hybrid* method to be able to restore any kind of defect, the contralateral (healthy) mirrored part must be replaced by a new tool able to provide the missing information also for non-unilateral defects. To date, a robust approach to deliver an adequate template for anatomical reconstruction is by exploiting statistical analysis, to gather and interpret information from a sufficiently large collection of samples belonging to the same class of shape (healthy cranial vaults, in this application). The starting collection of samples is usually known as Training Set (TS). By means of a statistical representation of typical shape variations for the models under consideration, it is possible to account for the anatomical structures' enormous complexity as well as their high interpersonal variability. In particular, Statistical Shape Analysis (SSA) [14,15] represents the most established statistical tool in medical image analysis [8,16–18], and it has been widely used in image segmentation, anatomical reconstruction, joint kinematic analysis, morphological abnormality investigation [19–21]; in addition, SSA represents a strong tool in providing the most likely full shape by starting from its a-priori partial knowledge [17,22–25]. Furthermore, SSA already proved its reliability as a template for cranial vault reconstruction [17].

Operatively, SSA encodes all the shape information learned from the TS into a Mean Shape and a series of its possible deformations, called Modes of Variation (MoVs). The resulting deformable model is called Statistical Shape Model or SSM. The SSM may be also seen as a constrained deformation within a precise domain of a reference shape (i.e., the Mean Shape) [26]. Both the reference shape and the deformation constraints (i.e., the deformation do-

main) are learned from the initial TS. Consequently, the construction of an adequate TS is critical since it defines the domain of the shape space and, consequently, all the shapes the SSM may create. In particular, the quality of the final model and its ability to describe a consistent shape space are severely affected by the extension and homogeneity of the TS. Although it may always seem true that the larger the TS, the greater its ability to describe different shapes, this statement only works if all training samples are mutually consistent; in other words, the training samples must describe the same anatomical structures that differ only in their shape characteristics, not in their medical condition, ethnicity, age, gender, and so on. For these reasons and considering the difficulties to find a wide number of homogeneous anatomies, usually the resulting SSM has a poor ability to describe a shape space wide enough to be able to fit a partially known anatomy ensuring a limited deviation between the original data and the deformed model. In our application, this means that a high user interaction would be required to properly reach a good matching between the defective model and the deformed template, which is a fundamental condition to avoid discontinuities and to gain a consistent reconstruction.

For this reason, the HyM3D method uses the SSM only to obtain the MPs, instead of exploiting the entire fitted model. As a consequence, the slight deviation between the fitted SSM and the a-priori known parts is no longer a major limitation. The continuity at the boundary of the cranial defect is here ensured by forcing the reconstructive surface through the BPs and the n-RNs.

2.3.1. Statistical shape model definition

The way to define the SSM heavily depends on how the training samples are organized. As said, in *Data Representation* section, the straightforward solution to represent complex shapes is by means of a Point Distribution Model (PDM) [10], i.e. a discrete description based on a set of points (named landmarks) distributed across the surface [8,9]. In biology, the statistical characterization of shape variations patterns based on Cartesian landmark coordinates, known as *Geometric Morphometrics*, is an approach grown out from early '900 and fully established with Bookstein starting from the '80s [27]. The great advantage in working with PDMs is that statistics on points are easily interpretable and have a physical significance; on the other hand, the high amount of data (i.e., the dense set of points) required to adequately describe complex 3D shapes makes it difficult to gather and analyze the whole set of information. To reduce the problem's dimensionality without losing generality, the typical approach to SSM definition is based on Principal Component Analysis (PCA) [28]. Using a PCA-based approach, it is possible to define the space of all possible shape deformations described by the set of the M samples $\{\Gamma^1 \Gamma^2 \dots \Gamma^M\}$ forming the training set. Each training shape Γ^i is represented as a PDM with a discrete set of landmarks \mathbf{x}^i . According to Eq. (1), Γ^i can be defined as:

$$\Gamma^i = \{ \mathbf{x}_k^i \mid \mathbf{x}_k^i \in \mathbb{R}^3, k = 1, \dots, N_i \} \quad (3)$$

where N_i is the number of points used to describe the shape Γ^i , and \mathbf{x}_k^i contains the 3 cartesian coordinates (Eq. (2)) of the k -th point.

Each shape Γ^i is properly rearranged by stacking the coordinates of each point k in a large ($3N_i$ elements) column vector $\bar{\mathbf{x}}^i$. Considering the global reference system in the x -, y - and z -axis:

$$\bar{\mathbf{x}}^i = [x_1^i \ x_2^i \ \dots \ x_{N_i}^i \ y_1^i \ y_2^i \ \dots \ y_{N_i}^i \ z_1^i \ z_2^i \ \dots \ z_{N_i}^i]^T \quad (4)$$

As a result, the column vector reported in Eq. (4) represents the $3N_i$ variables of a single observation Γ^i .

To apply the PCA, the whole training set has to be then organized in a matrix (**TS**) whose columns are the observations (i.e.,

the M shapes) and rows are the variables:

$$\mathbf{TS} = [\bar{\mathbf{x}}^1 \ \bar{\mathbf{x}}^2 \ \dots \ \bar{\mathbf{x}}^M] \quad (5)$$

For a correct definition of the \mathbf{TS} , i.e., for a correct definition of the raw dataset on which apply the PCA, it must be strictly assumed that the points are in *correspondence*, i.e., the points of all training samples are located at the corresponding position. In other words, it means that the k -th landmark x_k^i and x_k^j of two shapes Γ^i and Γ^j represents the same point. It is worth noting that the PDMs from which to derive the training samples could be, and usually are, described by a different number of points N_i . To obtain a proper \mathbf{TS} , such models need to be reworked to satisfy the *correspondence* assumption. When all the training samples are in correspondence, all the observations have the same number of rows N , and \mathbf{TS} is a $3N \times M$ matrix. Obviously, the larger N , the more complete the description of the variability of the initial training set; on the other hand, the larger N the more complex the correspondence problem becomes.

Finding a meaningful correspondence between shapes is one of the critical tasks of shape analysis [29]: a good correspondence enables to retrieve the correct information from the training set, because each row of the \mathbf{TS} , i.e. each variable, refers to a specific location across all the training samples.

Once the dataset \mathbf{TS} is properly defined, the direct calculation of the mean shape is possible by simply averaging over all M samples:

$$\bar{\mathbf{x}} = \frac{1}{M} \sum_{i=1}^M \bar{\mathbf{x}}_i \quad (6)$$

The covariance matrix \mathbf{S} is given by:

$$\mathbf{S} = \frac{1}{M-1} \sum_{i=1}^M (\bar{\mathbf{x}}_i - \bar{\mathbf{x}})(\bar{\mathbf{x}}_i - \bar{\mathbf{x}})^T \quad (7)$$

A typical PCA-based approach is usually used to provide an eigendecomposition on \mathbf{S} delivering the principal *Modes of Variation* (MoVs) Φ (matrix whose columns are the eigenvectors of the \mathbf{S} matrix) and their respective variances λ (vector containing the eigenvalues of the matrix \mathbf{S}). Operatively, the PCA returns the plausible deformations, delivered as directions (Φ) and related amplitudes (λ) of displacement, of every single point of the mean shape. It is now possible to approximate new valid shapes, i.e. new individuals belonging to the same *family* of shapes forming the \mathbf{TS} matrix, by a linear combination of the first c MoVs:

$$\mathbf{x} = \bar{\mathbf{x}} + \sum_{m=1}^c \alpha_m \sqrt{\lambda_m} \varphi_m \quad (8)$$

Where:

- $\bar{\mathbf{x}}$ is the mean shape as defined in Eq. (6).
- λ_m and φ_m are, respectively, the eigenvalues and eigenvectors of matrix \mathbf{S} ordered by their variances ($\lambda_1 \geq \dots \geq \lambda_c$).
- $\alpha \in R^c$ is a coefficients vector that permits to constrain the allowed variation to plausible shapes; usually, α is allowed to vary in the range $[-3; +3]$, which corresponds to a deformation that is 3 standard deviations away from the mean ($\alpha = 0$ means that the model is equal to the mean shape).
- c represents the number of significant eigenvalues. In the presented application, c is defined so that the accumulated variance (the numerator of Eq. (9)) reaches a certain ratio r of the total variance (the denominator of Eq. (9)). Common values of r are between 0.9 and 0.98. Henceforward, an r equal to 0.98 will be considered.

$$\frac{\sum_{i=1}^c \lambda_i}{\sum_{j=1}^{M-1} \lambda_j} = r \quad (9)$$

Following the mathematical framework presented in [30], the SSM defined in Equation 4.6 can be represented in matrix form:

$$\mathbf{x} = \mathbf{x}(\alpha) = \bar{\mathbf{x}} + \mathbf{UD}\alpha = \bar{\mathbf{x}} + \mathbf{Q}\alpha \quad (10)$$

Where $\mathbf{U} = (\varphi_1, \dots, \varphi_M)$ and $\mathbf{D} = (\sqrt{\lambda_1}, \dots, \sqrt{\lambda_M})$ are the matrices containing, respectively, the eigenvectors and the eigenvalues of the covariance matrix \mathbf{S} as defined in Eq. (7).

Eq. (8) and Eq. (10) represent a convenient mathematical representation of an anatomical healthy ROI, and they are able to generate new consistent shapes by simply varying the parameters in the vector α . In this application, Eq. (10) is used to infer the full shape of the defective model to be restored, predicting a likely healthy shape from given partial data by following the procedure described below in the section *How to find the MPs from the SSM: fitting the Mean Shape on the defective model*.

Though the whole procedure seems straightforward, the construction of the \mathbf{TS} matrix and, in particular, the establishment of the correspondences (i.e. the identification of the points belonging to different models but located at corresponding position) actually represents a critical step. Point correspondence is a crucial assumption to apply standard multivariate statistics to model a probability distribution over shapes because it enables proper data collection and interpretation, starting from the training samples. Therefore, the correspondence problem represents the most challenging part of the SSM construction [8] because the quality of the SSM itself is heavily influenced by the quality of the established correspondences. Since the manual landmarking approach is not appropriate when working with complex 3D shapes (due to the large number of points needed to produce an acceptable superimposition), several methods for the automatic detection of shape correspondences have been proposed in the literature [8]. All the proposed automatic algorithms perform a registration between PDMs: the most straightforward solution is to choose an arbitrary shape as a reference and warp it to all others by using a non-rigid point set registration. To date, the most established methods to perform such registration are based on Iterative Closest Point (ICP) algorithm [31,32] or, alternatively, on Coherent Point Drift (CPD) algorithm [33]. The main advantage of using non-rigid point set algorithms is that they treat correspondence as a variable to be estimated and not as an input (as happens, for instance, in the Procrustes-based algorithms). To overcome the bias caused by using an arbitrary reference shape, the procedure can be repeated a second time using the Mean Shape obtained by the SSM [34] or by using a symmetric version of the non-rigid registration (as presented in [35] with reference to ICP).

The most established approach based on non-rigid registration [8] in the specific application of the human skull proved to be insufficient when applied directly on the 3D model obtained from the CT data. Actually, due to the wide anatomical variability and the extreme complexity of the hard tissues in the cranial region, the method often fails to detect appropriate shape correspondences. To overcome these drawbacks, in [7] a methodological procedure to compute an SSM using a pair-wise registration based on an automatic detection of shape correspondences is presented. The procedure relies on a strategy for robust automatic detection of shape correspondence to properly rearrange the initial training dataset formed by a large number of cranial models delivered as PDMs; the aim is to build a \mathbf{TS} matrix that describes the same variability of the initial training set but properly shaped in order to enable a correct application of the SSA on the data. Requiring no user intervention, the number of samples in the Training Set can be increased at will to increase the variability, and therefore the accuracy, of the resulting parametric model. The ICP algorithm is used in [7] to align the initial training shapes. The best performance of the ICP with respect to the most established alternative

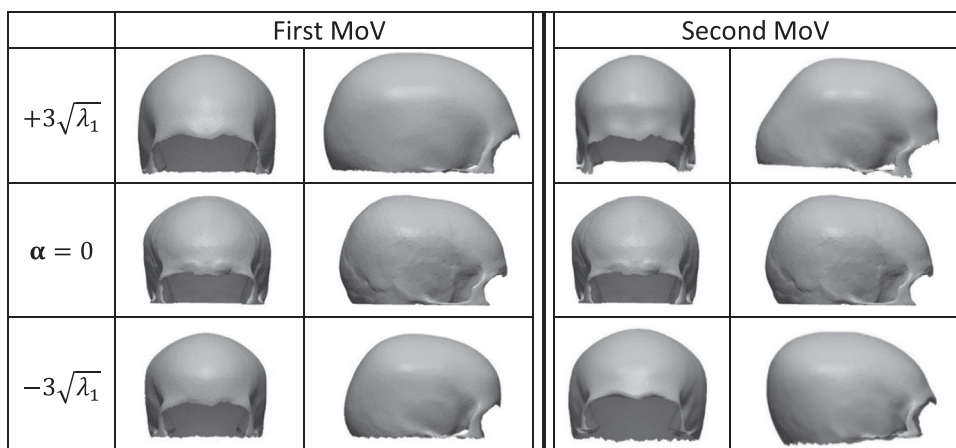


Fig. 4. The first two MoVs.

proposed in the literature, which is represented by the CPD [33], is well described in [36].

In this work, the algorithm described in [7] is followed to build the **TS**; since the procedure described in [7] uses PDMs as inputs (as for the HyM3D method) and requires no user interaction, it is integrated without any modifications in the procedure described in Fig. 2.

Once the **TS** is properly shaped, both the Mean Shape (Eq. (6)) and the covariance matrix **S** (Eq. (7)) can be defined. In SSA, to reduce the problem’s dimensionality without losing generality, the calculation of the eigenvectors φ_m and the eigenvalues λ_m of the covariance matrix **S** is actually performed by a *Singular Value Decomposition* (SVD) [37,38] on the mean-centered dataset matrix **L** instead of using the eigenanalysis on the covariance matrix **S**. **L** is obtained by mean-centering the matrix **TS**, i.e. by subtracting the variable averages from the data in **TS** (Eq. (11)).

$$\mathbf{L} = ((\bar{\mathbf{x}}^1 - \bar{\mathbf{x}}), \dots, (\bar{\mathbf{x}}^M - \bar{\mathbf{x}})) \tag{11}$$

The eigendecomposition applied on **S** yields the same results as the SVD performed on **L**, but the latter is preferred since it provides better numerical stability [8].

By performing the PCA to the **TS**, the first c significant MoVs with the respective variances are delivered. Based on our definition of c , they provide 98% of the total variance of all the instances contained in **TS**. Fig. 4 depicts the first two MoVs of the exocranial surface as resulting from the application of the SSA to the **TS**; the figure shows the maximum and minimum deformation according to φ_1 and φ_2 with respect to the mean shape ($\alpha = 0$).

In this application, the initial training set contains 100 healthy cranial exoskeletons (43 female, 57 male, average age= 32.6 years). The original anonymized CT images were downloaded in DICOM format from an online repository [39]. At a first stage, a selection of the patients was performed, to make the training set as uniform as possible; unfortunately, the anonymized images provided little information about each patient, so it was not possible to properly optimize the initial dataset. Despite that, the resulting SSM can still be considered as a first attempt to test the potentialities of the method. By working on the uniformity and size of the Training Set, the quality of the resulting SSM, and therefore the accuracy of the reconstruction, can be significantly improved. The choice of the size of the **TS** was guided by the consideration presented in the next section entitled *Statistical Shape Model Evaluation*.

The STL models have been obtained from the anonymized diagnostic images using specifically designed tools in Materialise Mimics® software (Materialise NV, Leuven, Belgium) for image segmentation and for exporting the STL models themselves. To

expedite the subsequent operations, each of the so-obtained STL models is roughly finished (removal of outliers and redundant regions). In order to keep the calculation cost limited, the number of points of each training neurocranium is decimated up to about 10,000–15,000 points.

As a result of the procedure presented in [7], the matrix **TS** (as defined in Eq. (5)) and the parametric representation of the SSM (Eq. (8)) are automatically provided.

A comprehensive assessment of the effectiveness of the delivered results along with an evaluation of the quality of the **TS** matrix and, consequently, of the quality of the correspondences established among the training samples, is reported in the following paragraph.

2.3.2. Statistical shape model evaluation

The most established approach for the SSM quality assessment is based on the work published by Davies in 2002 [40]. In this paper, the author proposed a methodological procedure to evaluate the general quality of an SSM identifying the properties that would ideally be required for such a model: the *Generalization ability*, the *Specificity*, and the *Compactness*. The author’s aim was indeed to compare different models constructed starting from the same training set rather than to propose an absolute measure of the quality of an SSM. As a consequence, to provide a more significant and objective evaluation of the quality of an SSM, many authors [8,41–44] have proposed alternative approaches over the years, especially for the calculation of the *Generalization ability* and the *Specificity*. The different approaches differ for the metric \mathcal{D} used to compare different shapes (see Eq. (12) and Eq. (13)). However, only the method for calculating the three factors that Davies described has evolved over time, while the basic ideas supporting the evaluation technique proved to be very robust and are, therefore, still valid in their original formulation. In this Section, an exhaustive description of the three properties is provided, and the approach followed in this application to calculate each of them is described and justified.

The first property, the *Generalization ability* \mathcal{G} , quantifies the capability of the SSM to reproduce a given model; in other words, \mathcal{G} measures the ability of the model to learn the characteristics of the *family* of shapes under consideration from a limited training set. It is estimated by performing a series of leave-one-out tests on the training set, measuring the distance of the omitted training shape Γ^i to its closest match $\Gamma_*^i(c)$ provided by the reduced SSM.

The *Generalization ability* is given as a function of the number c of the significant eigenvalues used to define the parametric model

(see Eq. (9) for the definition of c):

$$\mathcal{G}(c) = \frac{1}{N} \sum_{i=1}^M \mathcal{D}(\Gamma_*^i(c), \Gamma^i) \quad (12)$$

Lower values of \mathcal{G} indicate better SSMs. \mathcal{D} represents the metric used to compute the distance between the shapes: by varying \mathcal{D} , the significance of the difference changes. According to the approach presented in [42], the *Symmetric Mean* (SM) distance calculated between the nearest points is used in this paper as the \mathcal{D} metric. Using the SM calculated between the nearest points, instead of exploiting the same pairwise correspondences already defined during the **TS** definition, ensures to exclude from the evaluation any aspect regarding the registration process, thus providing only an assessment of the model's ability to match a given shape.

This approach also considers a normalization with respect to N (i.e. the number of the points of Γ_*^i and Γ^i). As a consequence, \mathcal{G} value is not just an index for direct comparison with other SSMs but also represents a measure of the fitting error (in *mm*) between a target shape and its closest reconstruction achievable with the SSM under consideration. Using this method and taking into account a sufficient number of leave-one-out tests, \mathcal{G} may be seen as an estimate of the expected fitting error (in *mm*) of the statistical model under consideration.

The second measure to evaluate an SSM is the *Specificity* \mathcal{S} that describes the model's ability to generate new consistent shapes, i.e. shapes belonging to the *family* of shapes under consideration. The measure is estimated by generating random parameters α ; the distance of each generated shape $\Gamma_{**}^k(c)$ to the closest match of the training set is then averaged over a large number of runs t . As the *Generalization ability*, the *Specificity* is provided as a function of the significant eigenvalues number c :

$$\mathcal{S}(c) = \frac{1}{t} \sum_{k=1}^n \min_{\{i=1, \dots, M\}} \mathcal{D}(\Gamma_{**}^k(c), \Gamma^i) \quad (13)$$

For the *Specificity*, the metric \mathcal{D} used in this application is the *Mean Absolute Distance* (MAD) between corresponding points to make the measurement robust and independent from the number of landmarks [41]. When comparing two SSMs obtained from the same **TS**, lower values of \mathcal{S} indicate better SSMs. It is worth noting that the $\mathcal{S}(c)$ gets worse as the c improves; although this may seem a counter-intuitive behavior (since it is expected that the quality of an SSM improves when its ability to encode a larger variability of the TS improves), it may be fully explained by keeping in mind that the more variety there is, the easier it is for the SSM to elude the members of the **TS**.

The last measure is the *Compactness* \mathcal{C} , which simply represents the cumulative variance of the model as calculated by PCA. In this application, the \mathcal{C} value is normalized by the total variance $\sum_{j=1}^{M-1} \lambda_j$:

$$\mathcal{C}(c) = \frac{\sum_{i=1}^c \lambda_i}{\sum_{j=1}^{M-1} \lambda_j} \quad (14)$$

A compact model (i.e. small value of \mathcal{C}) requires few parameters to encode a larger variability of the **TS**. So, contrary to the two previous measures, higher values of \mathcal{C} indicate better SSMs.

The just-defined values of $\mathcal{G}(c)$, $\mathcal{S}(c)$ and $\mathcal{C}(c)$ for the constructed SSM have been computed and reported in Figs. 5-7.

To calculate $\mathcal{G}(c)$, as many leave-one-out tests as the number of shape samples have been performed, so all the 100 shapes have been tested. The number of runs t carried out to calculate the $\mathcal{S}(c)$ is 10,000, as recommended by Davies in [45].

Despite $\mathcal{S}(c)$ and $\mathcal{C}(c)$ cannot be used as absolute measures of the quality of an SSM, $\mathcal{G}(c)$ can be interpreted, as said before in

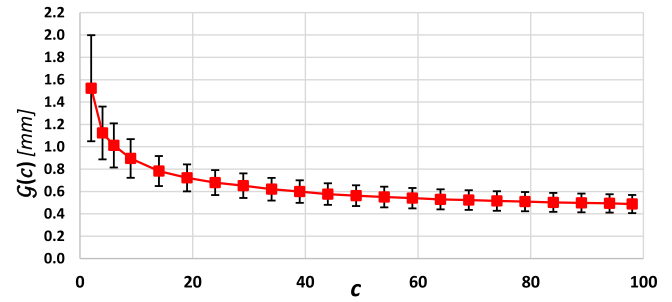


Fig. 5. Generalization ability.

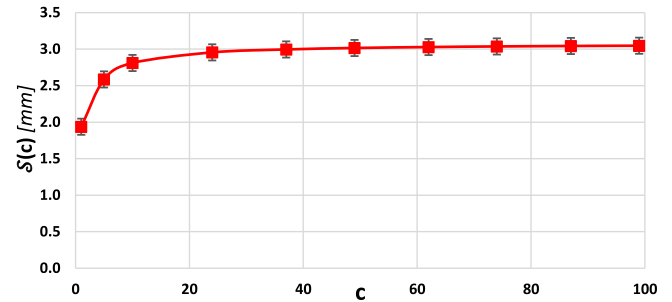


Fig. 6. Specificity.

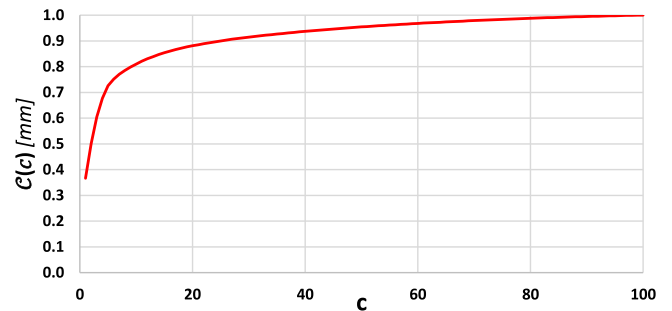


Fig. 7. Compactness.

this section, as an indication of the fitting error between the SSM and a target shape. Consequently, $\mathcal{G}(c)$ (Fig. 5) indicates that the SSM built in this application can match a target shape with an expected absolute mean error equal to 0.51 ± 0.09 *mm* by considering that c has been set equal to 73 to ensure an r equal to 0.98 (see Eq. (9)). It is important to note that the quality of a statistical model is directly correlated with the available amount of training data. As the training set is expanded, the resultant parametric model's accuracy and variability increase. Due to the data collection method, the availability of 3D anatomical models is, unfortunately, almost always inadequate since it is rare to get a suitably resolute diagnostic image of a healthy ROI. Furthermore, the required pre-processing (i.e. manual segmentation and model cleaning) is very cumbersome and time-consuming. As a consequence, the limitations imposed on the permitted deformation prevent the resulting SSM from accurately adjusting to new data. In addition, Fig. 8 shows that the higher the number of samples, the more difficult is to get better indices. Due to the flattening of the $\mathcal{G}(M)$ curve, more and more training samples are required to enhance the quality of the resulting SSM. The choice of 100 training samples is then justified by a trade-off between reaching good indices and the number of additional training samples required to obtain a significant improvement of the same indices.

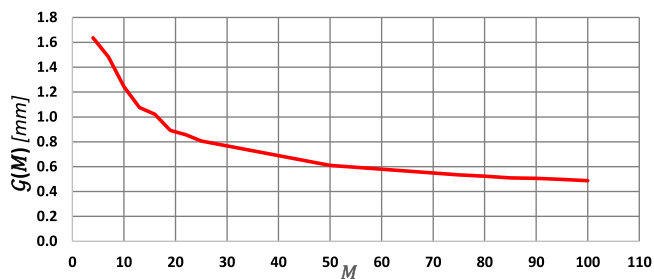


Fig. 8. Generalization ability by increasing the number of training samples.

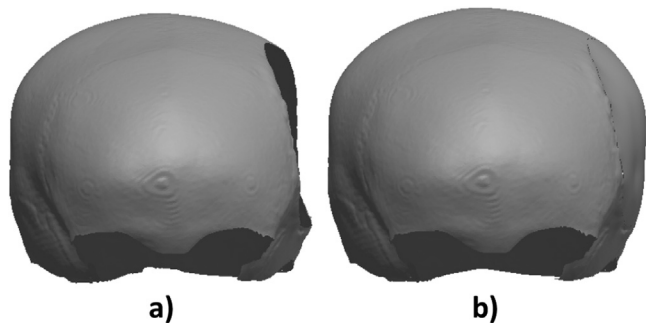


Fig. 9. The prior model x_g (a) constrains the possible resulting shapes x_c (b).

2.3.3. How to find the MPs from the SSM: fitting the mean shape on the defective model

In addition to the ability to generate new consistent shapes based on a set of representative training samples, SSMs have also been used to infer the full shape from partial data (Fig. 9). Whether the objective shape x is partially known, it can be used as prior knowledge to constraint the shape space described by the SSM.

The information available (namely the locations of the known points describing the model to be reconstructed) is given in form of $q < N$ entries: these entries are henceforward denoted as $x_g \in R^{3q}$. Related to the data x_g , the sub-vector $\bar{x}_g \in R^{3q}$ and sub-matrix $Q_g \in R^{3q \times M}$ can be defined from the full model's \bar{x} and Q by selecting the rows corresponding to the given entries only. It is necessary to know which entries in x_g correspond to which entries in x in order to select the correct rows from \bar{x} and Q . It is then possible to define:

$$x_g = x_g(\alpha) = \bar{x}_g + Q_g \alpha \tag{15}$$

where α is the only unknown parameter. By inverting Eq. (15):

$$\alpha = Q_g^{-1} (x_g - \bar{x}_g) \tag{16}$$

Since the vector $\alpha \in R^c$ is not affected by the actual number of points of the shapes involved (c depends on the MoVs and it is uniquely defined by defining r), it is possible to infer the un-defective model by using Eq. (10) with the α value provided by Eq. (16). The resulting shape, called x_c , represents the most likely (complete) shape according to the TS once given the initial partial data. In this application, it represents the most likely healthy cranial vault reproducing the known bone (Fig. 9). x_c is, then, the model useful for providing the MPs.

The computation of x_c can be easily included in the procedure presented in [5], as they share the same input x_g .

3. Results

The procedure to obtain the parametric model and to fit the Mean Shape onto the a-priori known model has been implemented

Table 1

The combinations of parameters n and m in each of the test cases addressed.

	$m=10$ mm	$m=25$ mm	$m=40$ mm	$m=80$ mm
$n=10$ rings	$n=10; m=10$	$n=10; m=25$	$n=10; m=40$	$n=10; m=80$
$n=40$ rings	$n=40; m=10$	$n=40; m=25$	$n=40; m=40$	$n=40; m=80$
$n=70$ rings	$n=70; m=10$	$n=70; m=25$	$n=70; m=40$	$n=70; m=80$

in Matlab® (MathWorks, Inc.) to make the integration with the original formulation (also implemented in Matlab®) easier. The algorithm automatically provides the matrix TS (as defined in Eq. (5)) and the SSM (Eq. (8)). The SSM only needs to be built once, and can then be integrated into the reconstruction process described in Fig. 2 which automatically provides the restored cranial vault by taking just the STL of the defective neurocranium to be reconstructed as input. The algorithm also requires two more input parameters (as discussed in the paragraph *The HyM3D method*):

- m , which represents the minimum distance (in mm) between the boundary loop and the outer ring of the MPs.
- n , which represents the number of points rings lying on the outer side of the boundary loop to create an overlapping region between the interpolating surface and the healthy bone.

Before facing the actual reconstruction task, several tests have been performed in order to define the best combination of the two parameters. This preliminary experimental campaign involved 15 models, including 5 real defective skulls, 9 real skulls with synthetic defects, and a synthetic skull with synthetic defects. Both unilateral and non-unilateral defects have been considered. The tests have been carried out by applying 12 times the algorithm to each of the 15 test cases with the parameters m and n combined as follows (Table 1):

The choice of the m and n values is defined as explained in the following. By choosing a minimum value of m equal to 10 mm, the MPs are very close to the boundary loop but far enough not to compromise the continuity of the reconstructed surface. Values lower than 10 mm would lead to interpolation centers too close to the boundary loop. This situation is to be avoided since it would lead to the same continuity problems as in the typical *Template-based* approaches. In these cases, traditional *Surface Interpolation-based* is suitable for a consistent reconstruction. On the other hand, the maximum value of m (80 mm) has been chosen because it guarantees to have no MPs, i.e. to consider a pure *Surface Interpolation-based* approach. For these reasons, values lower than 10 mm and greater than 80 mm are not significant for the parameter m . Fig. 10(a) and Fig. 10(b) depict the interpolating surface passing through the centers of interpolation (shown in black) defined with, respectively, $m = 10$ and $m = 80$. In both Figures, n is equal to 10.

Regarding the n value, it relates to the thickness of the overlapping region between the interpolating surface and the healthy bone: the larger n the more extensive the overlapping region.

Fig. 10(c) and Fig. 10(d) show the interpolating surface passing through the centers resulting from, respectively, $n = 10$ and $n = 40$. In both Figures, m is equal to 10.

As for m , values lower than $n = 10$ or greater than $n = 40$ proved to be non-significant for the parameter n . In particular, the resulting reconstruction has proven not to be much sensitive to small variations of the parameter n , and imposing values lower than 10 would be equivalent to imposing $n = 10$. Obviously, $n = 0$ has been not taken into consideration because it cannot ensure the continuity of the curvature between the healthy bone around the defect and the reconstructed patch.

The tests showed consistent results in all the considered 15 case studies.

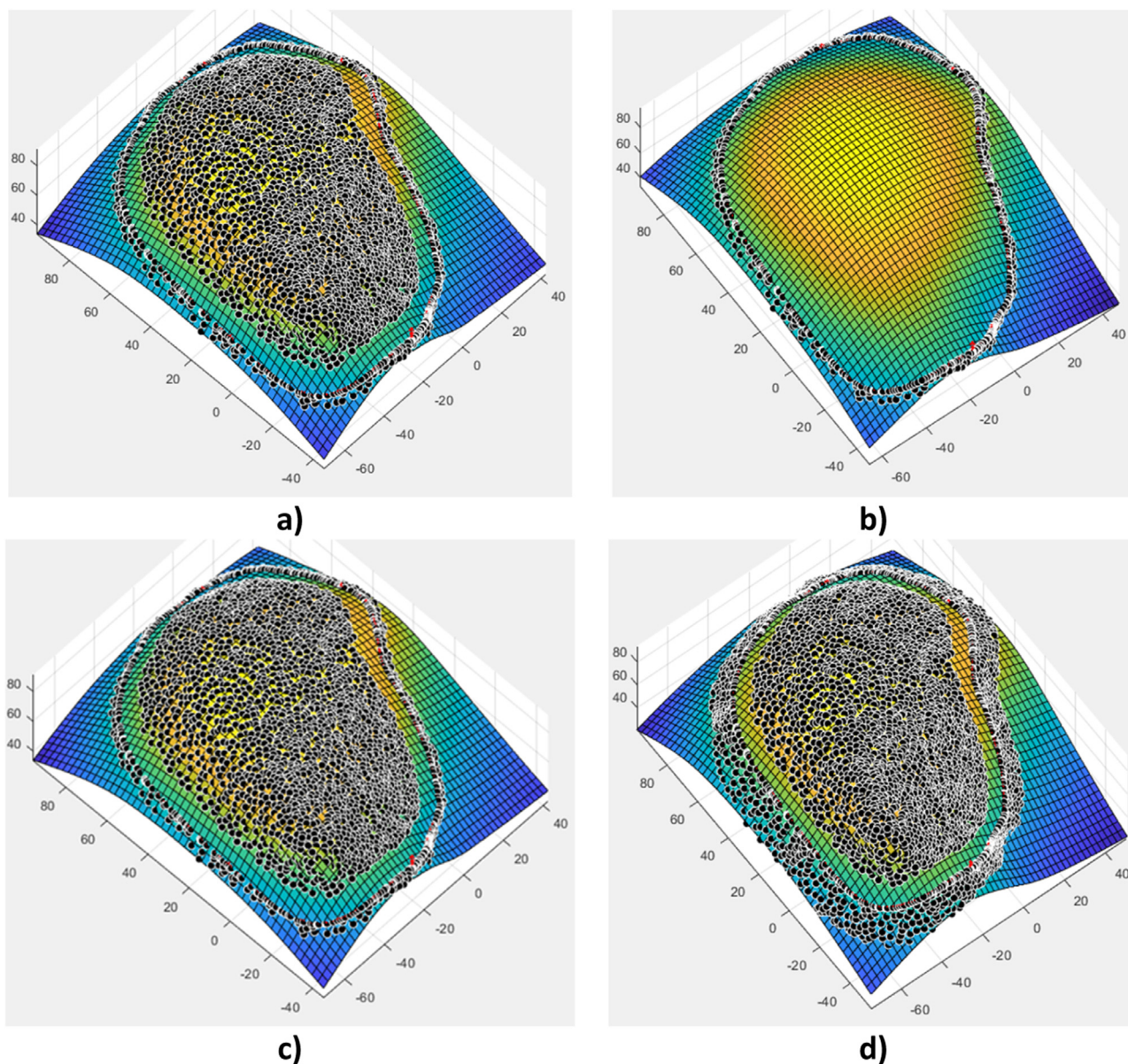


Fig. 10. The reconstructed surface by varying the interpolation centers. The outer rim is formed by the n -RNs and the BPs while the inner points are the MPs. (a) $n = 10$ and $m = 10$; (b) $n = 10$ and $m = 80$; (c) $n = 10$ and $m = 10$; (d) $n = 40$ and $m = 10$.

In the following, a selection of 4 representative models is presented and discussed in detail. The discussed models are shown in Table 2 and include:

- TC#1 and TC#2 which are, respectively, a synthetic and perfectly symmetric skull and a real skull. Both have a large synthetic defect that crosses (i.e. extends beyond) the *sagittal plane*.
- TC#3 and TC#4 which are real defective skulls with, respectively, a purely unilateral large defect and a defect that crosses the *sagittal plane*.

Tables 3–6 show the results of the test campaign carried out on the four case studies presented in Table 2. The results are evaluated using the AV index and the AV_{point} map [5,6,46]. These indices are able to deliver a quantitative assessment of the restored model regardless of what the shape of the cranial vault had been before the defect. AV represents the mean distances between each point of the restored skull with respect to its closest tessellated surface triangle of the mirrored configuration of the restored skull itself.

Consequently, AV provides a quantitative evaluation of the overall skull asymmetry: small value of the AV index means a symmetrical reconstruction and, thus, an acceptable outcome. AV_{point} is, instead, the point-value of the AV provided as a colormap on the restored cranial vault: abrupt changes in the AV_{point} colormap suggest possible macroscopic discontinuities at the connection between the bone and the patch. It is worth remarking that the AV index and the AV_{point} map enable an evaluation both in terms of symmetry and in terms of continuity between the patch and the surrounding healthy bone which can be applied also when the original healthy shape is completely unknown, which is, by far, the most common situation.

According to these indices, the results show that the quality of the reconstruction heavily depends on the m value, while it is little influenced by the n one. In particular, the best reconstruction can be achieved by imposing a low value of m , i.e. by minimizing the distance between the MPs and the boundary loop. But, as can be seen in Table 4, a too-low value of m could lead to worse results

Table 2
The four test cases discussed in detail.

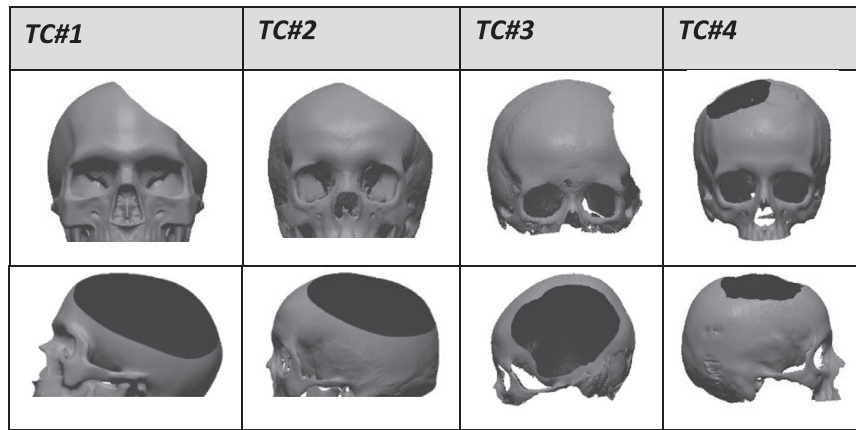


Table 3
The resulting AV and AV_{point} for TC#1.



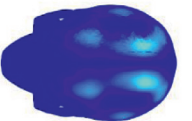
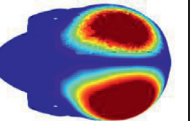


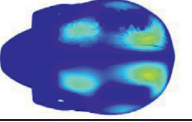
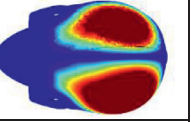


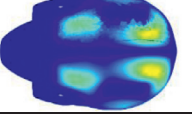
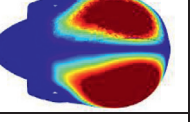
TC#1	$m=10\text{ mm}$	$m=25\text{ mm}$	$m=40\text{ mm}$	$m=80\text{ mm}$
$n=10\text{ rings}$				
	AV = 0.000 mm	AV = 0.058 mm	AV = 0.399 mm	AV = 2.043 mm
$n=40\text{ rings}$				
	AV = 0.000 mm	AV = 0.130 mm	AV = 0.611 mm	AV = 2.596 mm
$n=70\text{ rings}$				
	AV = 0.003 mm	AV = 0.125 mm	AV = 0.666 mm	AV = 2.600 mm

Table 4
The resulting AV and AV_{point} for TC#2.

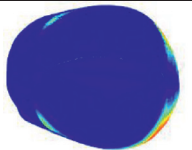
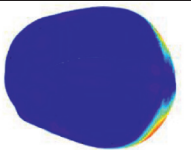
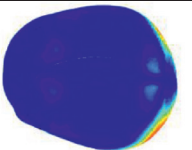
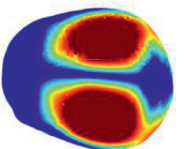
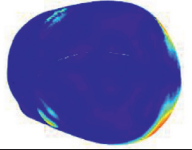
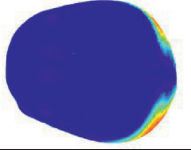
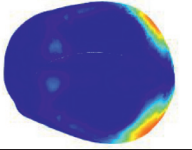
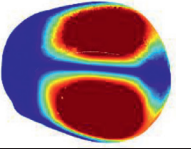
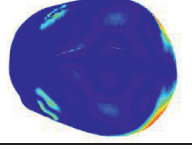
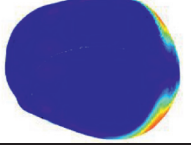
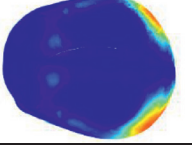
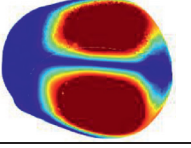
TC#2	$m=10\text{ mm}$	$m=25\text{ mm}$	$m=40\text{ mm}$	$m=80\text{ mm}$
$n=10\text{ rings}$				
	AV = 0.173 mm	AV = 0.154 mm	AV = 0.291 mm	AV = 2.761 mm
$n=40\text{ rings}$				
	AV = 0.392 mm	AV = 0.171 mm	AV = 0.498 mm	AV = 3.500 mm
$n=70\text{ rings}$				
	AV = 0.533 mm	AV = 0.163 mm	AV = 0.503 mm	AV = 3.536 mm

Table 5
The resulting AV and AV_{point} for TC#3.

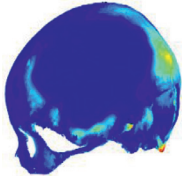
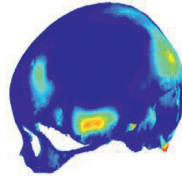
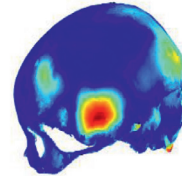
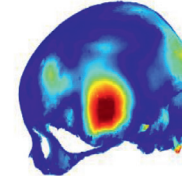
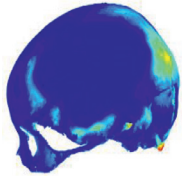
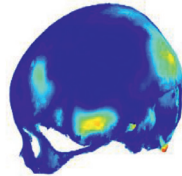
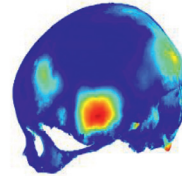
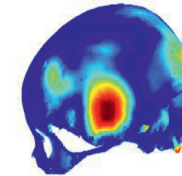
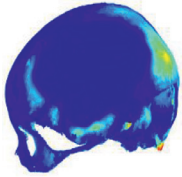
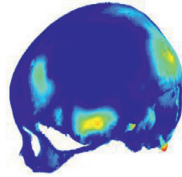
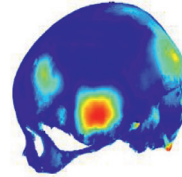
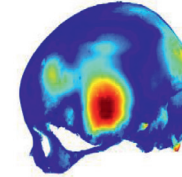
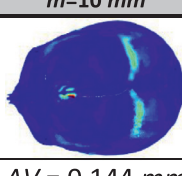
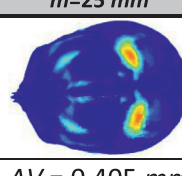
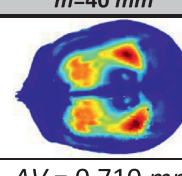
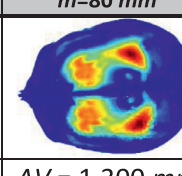
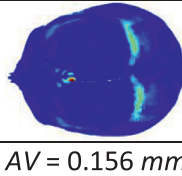
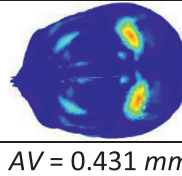
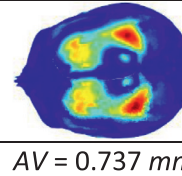
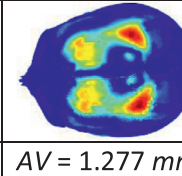
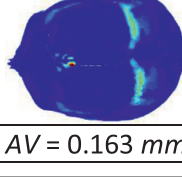
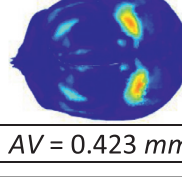
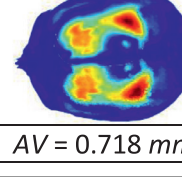
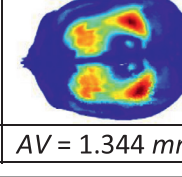
TC#3	<i>m</i> =10 mm	<i>m</i> =25 mm	<i>m</i> =40 mm	<i>m</i> =80 mm
<i>n</i> =10 rings				
	AV = 0.144 mm	AV = 0.405 mm	AV = 0.710 mm	AV = 1.300 mm
<i>n</i> =40 rings				
	AV = 0.156 mm	AV = 0.431 mm	AV = 0.737 mm	AV = 1.277 mm
<i>n</i> =70 rings				
	AV = 0.163 mm	AV = 0.423 mm	AV = 0.718 mm	AV = 1.344 mm

Table 6
The resulting AV and AV_{point} for TC#4.

TC#4	<i>m</i> =10 mm	<i>m</i> =25 mm	<i>m</i> =40 mm	<i>m</i> =80 mm
<i>n</i> =10 rings				
	AV = 0.144 mm	AV = 0.405 mm	AV = 0.710 mm	AV = 1.300 mm
<i>n</i> =40 rings				
	AV = 0.156 mm	AV = 0.431 mm	AV = 0.737 mm	AV = 1.277 mm
<i>n</i> =70 rings				
	AV = 0.163 mm	AV = 0.423 mm	AV = 0.718 mm	AV = 1.344 mm

in those cases where the template is not able to adequately follow the defective model: the coarse alignment between the MPs and the other interpolation centers can cause curvature discontinuities on the surface if *m* is too small, i.e. no sufficient distance is left between the boundary loop and the outer ring of the MPs. As said before in this section, this situation leads to the typical problems of pure *Template-based* approaches. For these reasons, an optimal value of *m* can be found only after an initial tuning of the parameter, experimentally assessed on the defective model under consideration. However, it can be assumed that, according to the reported

results, the optimal value of *m* falls between 10 and 25 mm (see [Tables 3-6](#)). This could be seen as a limitation of the devised algorithm, but it must be considered that a *trial-and-error* approach is commonly exploited in Reverse Engineering methods to find the best parameters definition because usually there is not sufficient a-priori information able to provide such parameters.

Regarding *m* = 80, it is worth to note that the results clearly underline that the reconstruction obtained without considering the MPs (therefore following a pure *Surface interpolation-based* approach) leads to questionable reconstructions in all the addressed

cases. This confirms that considering the MPs actually entails a relevant improvement over the *Surface Interpolation-based* approach.

Regarding the n value, as already mentioned, the results show that it has little influence on the quality of the reconstruction. However, in all the case studies the reconstruction worsens slightly if n increases. Probably, a high value of n over-constrains the interpolating surface that is less able to adapt accurately to interpolation centers.


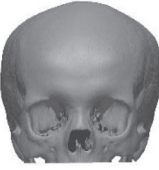
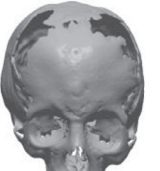

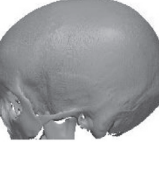
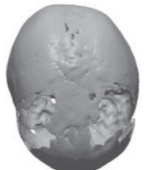
3.1. Evaluation of the proposed algorithm

In order to evaluate the quality of the reconstruction carried out by means of the HyM3D method, 50 test cases have been considered. The aim is to assess the quality of the reconstruction provided by the algorithm by retrieving the MPs from the SSM. The 50 test cases include neither the models considered in the previous Section nor the ones included in the training set.

In the following, the results of three representative cases, selected among all the test cases, are discussed in detail (see Table 7 and Figs. 11(a)-13(a)):

- TC#1 is a complete and perfectly symmetric synthetic skull.
- TC#2 is a real healthy skull.
- TC#3 is a real bilateral defective skull.

Table 7
Starting models for the discussed test cases.

TC#1	TC#2	TC#3
		
		

TC#1 and TC#2 are the same skulls presented in [5]. For each of the complete skulls (TC#1 and TC#2), artificial bilateral defects are modeled: the resulting models are named TC#1*

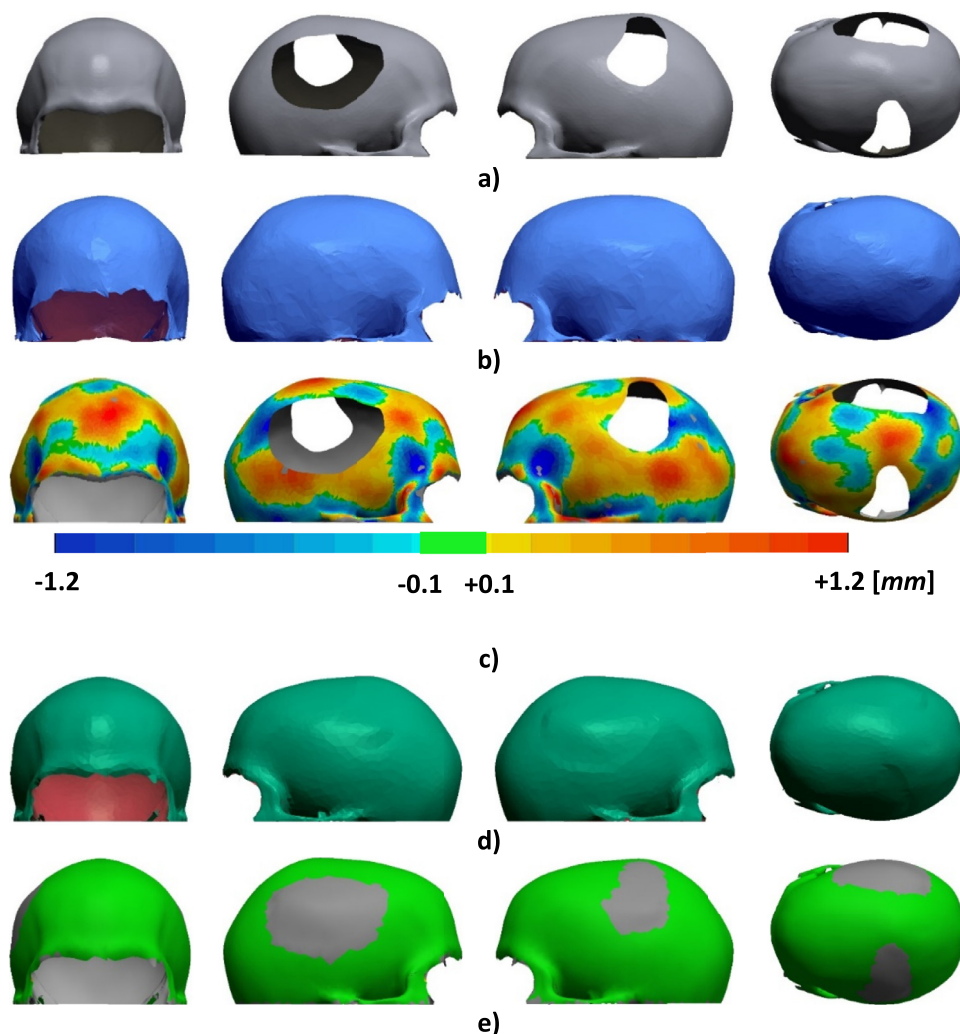


Fig. 11. Test Case TC#1* – (a) The defective model; (b) The fitted SSM; (c) Deviation map between (a) and (b); (d) The reconstruction provided by the proposed algorithm; (e) Deviation map between (d) and (a).

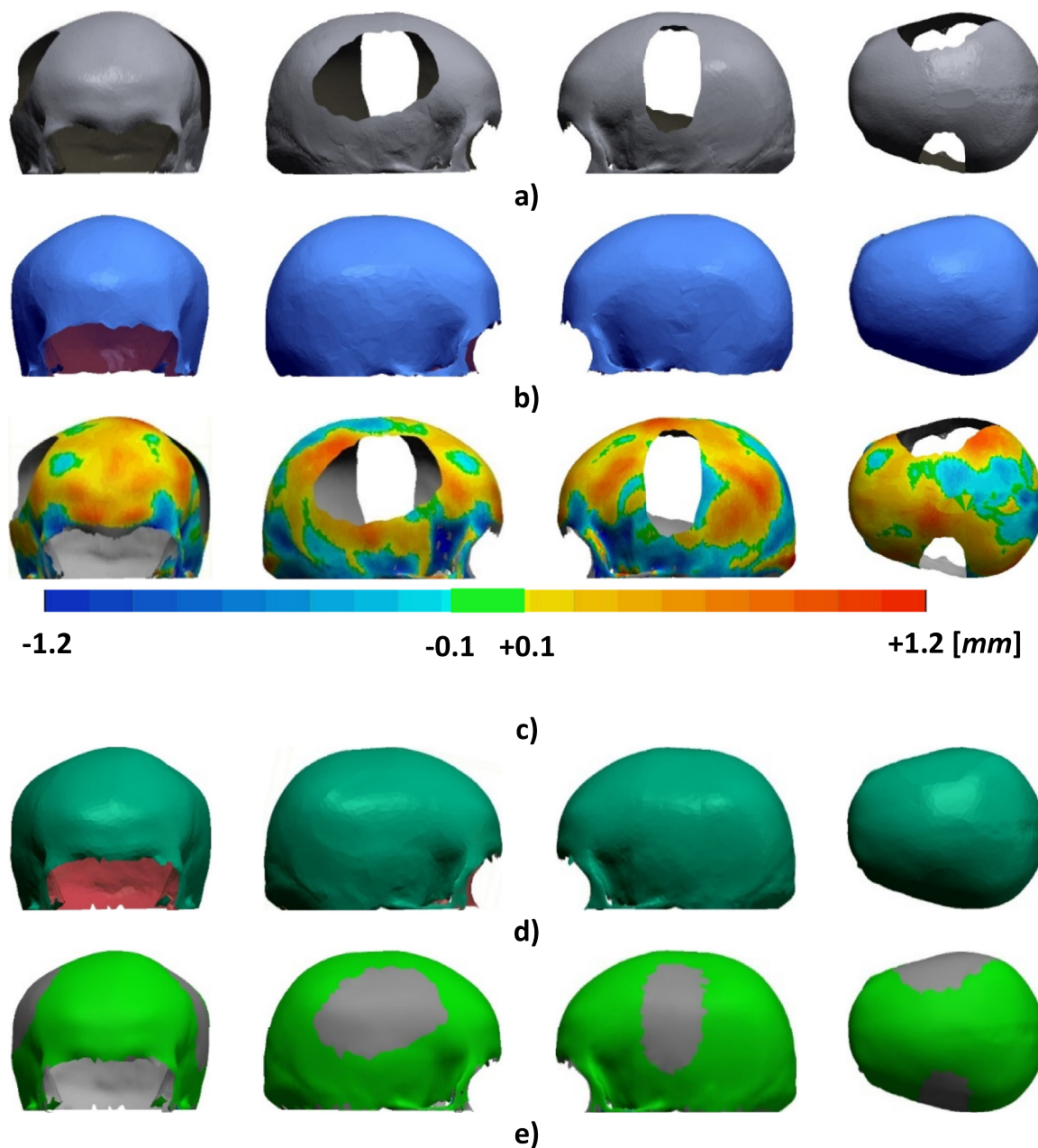


Fig. 12. Test Case TC #2* – (a) The defective model; (b) The fitted SSM; (c) Deviation map between (a) and (b); (d) The reconstruction provided by the proposed algorithm; (e) Deviation map between (d) and (a).

and TC#2*. Being a defective model, TC#3 is not further modified. In all the reported cases, the area of each defect (real or synthetic) is greater than 100 cm², so they can be considered *large defects* according to [12].

As far as procedure inputs are concerned, they are imposed, according to the previous section, as follows: $m = 18\text{ mm}$ and $n = 10$ rings. In particular, the m value is set equal to 18 mm after an initial tuning, because it has proven to be a trade-off value between the quality of the reconstruction and the robustness of the procedure in all the cases.

The results of the evaluation process are reported in Table 8 and Figs. 11-13. Along with the defective models to be reconstructed, Figs. 11(a)-13(a), Figs. 11(b)-13(b) and Figs. 11(c)-13(c) show, respectively, the fitted SSMs and the deviation map between the defective model (a) and its respective fitted SSM (b). The deviation

Table 8
AV values for all the unilateral test cases discussed.

Test Cases	Undeformed	Reconstructed
#1*	0.000 mm	0.003 mm
#2*	0.945 mm	1.130 mm
#3	N.A.	1.326 mm

maps depict, point by point, the Euclidian distances measured between correspondent points. It is worth underlining that the deviation maps confirm the expected absolute mean error between the fitted SSM and the target model discussed in the section *Statistical Shape Model Evaluation*: in fact, the expected error has been computed to be approximately $0.51 \pm 0.9\text{ mm}$, very close to the val-

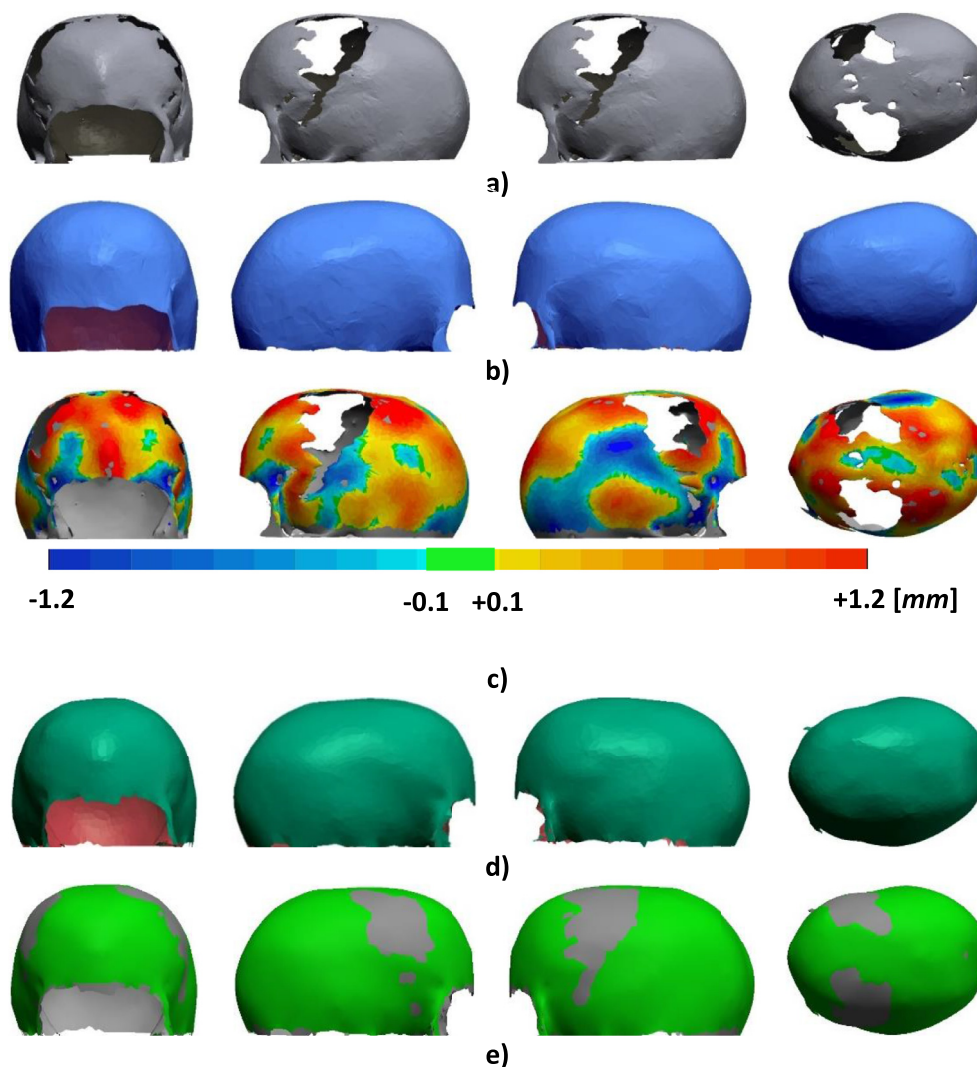


Fig. 13. Test Case #3 – (a) The defective model; (b) The fitted SSM; (c) Deviation map between (a) and (b); (d) The reconstruction provided by the proposed algorithm; (e) Deviation map between (d) and (a).

ues measured in the reported cases (i.e., respectively, 0.63 mm, 0.49 mm, and 0.68 mm).

The fitting errors shown in Figs. 11(c)–13(c) clearly demonstrate that performing the reconstruction through a typical *Template-based* approach (namely extrapolating from the SSM the full points-set that falls into the boundary loop) can lead to a distance up to 2.5 mm between the outer rim of the reconstructed patch and the edge of the surrounding bone. This condition results, as expected, in a lack of continuity between patch and bone which must be fixed by the operator through a series of manual time-consuming and cumbersome operations: as widely discussed in this paper, this actually represents the main limitation of the *Template-based* methods.



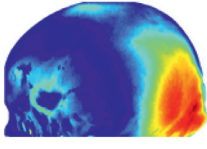
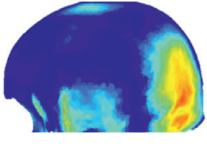
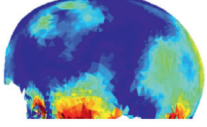
On the contrary, performing the reconstruction by using the proposed algorithm it is possible to overcome these shortcomings: Figs. 11(d)–13(d) and Figs. 11(e)–13(e) show, respectively, the reconstruction provided by the devised algorithm and the deviation maps between each defective model (a) and the reconstructed model (d). In particular, Figs. 11(e)–13(e) show that the reconstruction is perfectly superimposed on the known part of the skull to be reconstructed: by retrieving the BPs and *n*-RNs directly from the defective model, the algorithm is able to provide a restored cranial vault perfectly matching the actual model to be reconstructed without requiring time-consuming manual operations.

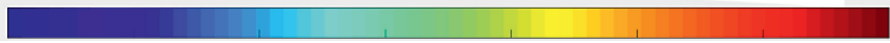
In the following, the results attained by the reconstruction strategy based on the SSM are further evaluated by means of the *AV* index and the AV_{point} map. The computed *AV* index is reported in Table 8 for the above-mentioned test cases. Where the comparison between the reconstructed model and the original healthy one is possible (i.e., for TC#1* and TC#2*), *AV* shows a value for the restored skulls very close to that of the originally known shapes, proving the effectiveness of the reconstruction delivered by the algorithm. With regard to TC#3, whose original shape is not known, the reconstruction achieves an *AV* index comparable with the *AV* computed for the undefective real model TC#2, which demonstrates the ability of the procedure to deliver consistent results.

The results also show that exploiting an external source as a template cannot ensure reconstructed models with an *AV* even lower than the original ones, as was the case in the *mirroring-based* reconstruction (see [5]). Actually, this is an expected result: while a reconstruction driven by the contralateral part leads obviously to a maximization of the similarity of the two halves, there are no constraints able to ensure symmetry when the external template is exploited to retrieve the MPs.

With regard to the AV_{point} , the absence of abrupt changes in the colormaps reported in Table 9 shows the lack of any kind of discontinuities or asymmetries at the interface between the healthy

Table 9
 AV_{point} maps for the discussed test cases.

	<i>Undefective</i>	<i>Reconstructed</i>
#1		
#2		
#3	N.A.	



0mm 1 2 3 4 5 6 7

skull and reconstructive patch for all three test cases. As a consequence, both AV and AV_{point} prove the effectiveness of the delivered reconstruction.

Dealing with the computational time to achieve the digital cranial restoration starting from the properly modified STL, it is closely related to the resolution of the surface model (number of vertices forming the STL file). For the addressed test cases, the computational time resulted to be between 30 s and 2 min for point sets varying from 4000 to 10,000 points. The algorithm is tested with a CPU Intel® Core™ i7-4712HQ/2.3 GHz and 16 GB RAM.

4. Conclusions and final remarks

The increasingly powerful and specialized CAx tools for handling complex geometries, such as anatomical ones, are representing a breakthrough in clinical practice. Especially in cranioplasty, the capability to make reliable simulations as well as to design the actual implant at the preoperative stage using the patient’s diagnostic images has proven to be worthwhile, both in terms of effectiveness and costs.

To date, one of the hardest tasks in cranioplasty surgery is the pre-operative virtual design of a corrective cranial plate. To ensure an acceptable aesthetical and functional outcome, such a design must be based on a proper anatomical reconstruction usually done in virtual environments by skilled operators.

Several techniques have been developed for cranial vault digital reconstruction, but all of them share some drawbacks that limit their applicability (e.g. too complex or time-consuming operations or incorrect resulting geometries). The limitations are mainly related to the lack of information in the missing area and the complexity of the shape that must be restored. Consequently, a convincing solution able to ensure an easily automatable procedure with a consistent shape reconstruction is not yet available.

To overcome these drawbacks, a novel hole-filling procedure for the restoration of defective cranial vaults has been presented, suited for both unilateral and non-unilateral large defects.

The procedure works automatically starting from the external poly-faces of the defective neurocranium, leaving to the user only the selection of the hole to be repaired by clicking one point on its edge. Being landmarks-independent and avoiding any patch adaptation, the devised procedure represents a valid alternative to the existing approaches in terms of user’s burden, requiring less time-consuming and less cumbersome operations.

The innovative idea is to exploit a properly defined template to obtain some meaningful points (named MPs) in the missing or deformed region, with the aim to guide the subsequent reconstruction carried out by a *Surface Interpolation-based* technique. This approach makes it possible to overcome the shortcomings of the typical *Surface Interpolation-based* technique, which usually leads to a non-consistent shape: usually, the reconstructed patch results too flat due to the lack of centers of interpolation inside the defective region.

With regard to the template, a procedure able to ensure a reliable automatic construction of the SSM starting from a training set of healthy ROI has been implemented in the algorithm. Since it does not require any manual operation, the number of samples in the training set can be increased at will, without time-consuming or heavy and tedious operations required from the user. This allows for a training set with a larger population and, consequently, a more precise template for improving the ability to reproduce the wide interpersonal variability of the anatomical structures.

Several case studies have been faced to assess the effectiveness and reliability of the devised procedure. Since the quality of the reconstruction is strictly related to the aesthetical outcome, the evaluation method aims to assess the quality of the procedure considering those criteria that mainly affect aesthetics, i.e. the symmetry of the resulting skull and the continuity between the reconstructed patch and the surrounding bone.

According to the proposed evaluation method, the novel procedure leads to a consistent aesthetic outcome, also in the case of non-unilateral defects.

In addition, the test cases confirm that the reconstruction driven by the MPs enables to overcome the limitations of both the *Surface Interpolation-based* and the *Template-based* techniques, en-

asuring the cranial surface continuity and the resulting shape consistency without time-consuming user operation.

Considering the specific procedure here proposed, several aspects to be improved can be identified.

First of all, it is specially developed for the cranial vault. Because of the high complexity of the anatomy structures, it is difficult to provide a methodology reliable for all applications. Despite that, the possibility to extend the applicability of the proposed approach to different anatomies may deserve further investigations.

In addition, future developments could address the application of the devised algorithm to reconstruct missing areas from incomplete acquired 3D data in other fields, such as cultural heritage or industrial ones. From this point of view, the proposed approach could represent a powerful tool to be included, for instance, in the traditional Reverse Engineering process.

Future work should also concern the optimization of the whole procedure, to make it more robust given the wide variability of the input models. In order to improve the applicability of the procedure by making it fully automatic, future efforts should concentrate on the pre-processing steps like, for instance, the diagnostic images segmentation and the subsequent STL preparation (cleaning of the model and cranial vault isolation). In addition, an improvement of the SSM could be feasible by expanding the training set so to increase its ability to match the defective model.

Declaration of Competing Interest

The authors declare no conflict of interest.

References

- [1] E.M.S. Toh, A.A. Thenpandian, A.S.C. Foo, J.J.Y. Zhang, M.J.R. Lim, C.P. Goh, N. Dinesh, S.V. Vedicherla, M. Yang, K. Teo, T.T. Yeo, V.D.W. Nga, Clinical outcomes of 3d-printed bioresorbable scaffolds for bone tissue engineering—a pilot study on 126 patients for burrhole covers in subdural hematoma, *Biomedicine* 10 (2022) 2702, doi:10.3390/biomedicine10112702.
- [2] G. Rosenthal, I. Ng, S. Moscovici, K.K. Lee, T. Lay, C. Martin, G.T. Manley, Polyetheretherketone implants for the repair of large cranial defects, *Neurosurgery* 75 (2014) 523–529, doi:10.1227/NEU.0000000000000477.
- [3] Y. Volpe, R. Furferi, L. Governi, F. Ucheddu, M. Carfagni, F. Mussa, M. Scagnet, L. Genitori, Surgery of complex craniofacial defects: a single-step AM-based methodology, *Comput. Methods Programs Biomed.* 165 (2018) 225–233, doi:10.1016/j.cmpb.2018.09.002.
- [4] F. Buonamici, R. Furferi, L. Genitori, L. Governi, A. Marzola, F. Mussa, Y. Volpe, Reverse engineering techniques for virtual reconstruction of defective skulls: an overview of existing approaches, *Comput. Aided Des. Appl.* 16 (2018) 103–112, doi:10.14733/cadaps.2019.103-112.
- [5] A. Marzola, L. Governi, L. Genitori, F. Mussa, Y. Volpe, R. Furferi, A semi-automatic hybrid approach for defective skulls reconstruction, *Comput. Aided Des. Appl.* 17 (2019) 190–204, doi:10.14733/cadaps.2020.190-204.
- [6] L. di Angelo, P. di Stefano, L. Governi, A. Marzola, Y. Volpe, A robust and automatic method for the best symmetry plane detection of craniofacial skeletons, *Symmetry* 11 (2019) 245 Basel, doi:10.3390/sym11020245.
- [7] A. Marzola, M. Servi, Y. Volpe, A reliable procedure for the construction of a statistical shape model of the cranial vault, in: Rizzi, C., Andrisano, A.O., Leali, F., Gherardini, F., Pini, F., Vergnano, A. (eds) *Design Tools and Methods in Industrial Engineering*. ADM 2019. Lecture Notes in Mechanical Engineering, Springer, Cham (2020) 788–800, doi:10.1007/978-3-030-31154-4_67.
- [8] T. Heimann, H.P. Meinzer, Statistical shape models for 3D medical image segmentation: a review, *Med. Image Anal.* 13 (2009) 543–563, doi:10.1016/j.media.2009.05.004.
- [9] F.L. Bookstein, Landmark methods for forms without landmarks: morphometrics of group differences in outline shape, *Med. Image Anal.* 1 (1997) 225–243, doi:10.1016/S1361-8415(97)85012-8.
- [10] T.F. Cootes, C.J. Taylor, D.H. Cooper, J. Graham, Training models of shape from sets of examples, in: *BMVC92*, Springer London, London, 1992, pp. 9–18, doi:10.1007/978-1-4471-3201-1_2.
- [11] D.G. Kendall, A Survey of the Statistical Theory of Shape, *Stat. Sci.* 4 (1989), doi:10.1214/ss/1177012582.
- [12] C.S. Chong, H. Lee, A.S. Kumar, Automatic hole repairing for cranioplasty using bézier surface approximation, *J. Craniofac. Surg.* 17 (2006) 344–352, doi:10.1097/00001665-200603000-00024.
- [13] J.C. Carr, W.R. Fright, R.K. Beatson, Surface interpolation with radial basis functions for medical imaging, *IEEE Trans. Med. Imaging* 16 (1997) 96–107, doi:10.1109/42.552059.
- [14] T.F. Cootes, C.J. Taylor, D.H. Cooper, J. Graham, Active shape models—their training and application, *Comput. Vis. Image Underst.* 61 (1995) 38–59, doi:10.1006/cviu.1995.1004.
- [15] V. Blanz, T. Vetter, A morphable model for the synthesis of 3D faces, in: *Proceedings of the 26th Annual Conference on Computer Graphics and Interactive Techniques SIGGRAPH '99*, ACM Press, 1999, pp. 187–194, doi:10.1145/311535.311556. New York, USA.
- [16] T. Heimann, B. van Ginneken, M.A. Styner, Y. Arzhaeva, V. Aurich, C. Bauer, A. Beck, C. Becker, R. Beichel, G. Bekes, F. Bello, G. Binnig, H. Bischof, A. Bornik, P. Cashman, Y. Chi, A. Cordova, B.M. Dawant, M. Fidrich, J.D. Furst, D. Furukawa, L. Grenacher, J. Hornegger, D. Kainmuller, R.I. Kitney, H. Kobatake, H. Lamecker, T. Lange, J. Lee, B. Lennon, R. Li, S. Li, H.P. Meinzer, G. Nemeth, D.S. Raicu, A.M. Rau, E.M. van Rikxoort, M. Rousson, L. Rusko, K.A. Saddy, G. Schmidt, D. Seghers, A. Shimizu, P. Slagmolen, E. Sorantin, G. Soza, R. Susomboon, J.M. Waite, A. Wimmer, I. Wolf, Comparison and evaluation of methods for liver segmentation from CT datasets, *IEEE Trans. Med. Imaging* 28 (2009) 1251–1265, doi:10.1109/TMI.2009.2013851.
- [17] M.A. Fuessinger, S. Schwarz, C.P. Cornelius, M.C. Metzger, E. Ellis, F. Probst, W. Semper-Hogg, M. Gass, S. Schlager, Planning of skull reconstruction based on a statistical shape model combined with geometric morphometrics, *Int. J. Comput. Assist. Radiol. Surg.* 13 (2018) 519–529, doi:10.1007/s11548-017-1674-6.
- [18] E.A. Audenaert, J. van Houcke, D.F. Almeida, L. Paelinck, M. Peiffer, G. Steenackers, D. Vandermeulen, Cascaded statistical shape model based segmentation of the full lower limb in CT, *Comput. Methods Biomech. Biomed. Eng.* 22 (2019) 644–657, doi:10.1080/10255842.2019.1577828.
- [19] C.S. Mendoza, N. Safdar, K. Okada, E. Myers, G.F. Rogers, M.G. Linguraru, Personalized assessment of craniostylosis via statistical shape modeling, *Med. Image Anal.* 18 (2014) 635–646, doi:10.1016/j.media.2014.02.008.
- [20] W. Keustermans, T. Huysmans, F. Danckaers, A. Zarowski, B. Schmelzer, J. Sibbers, J.J.J. Dirckx, High quality statistical shape modelling of the human nasal cavity and applications, *R. Soc. Open Sci.* 5 (2018) 181558, doi:10.1098/rsos.181558.
- [21] J.T. Lynch, M.T.Y. Schneider, D.M. Perriman, J.M. Scarvell, M.R. Pickering, M. Asikuzzaman, C.R. Galvin, T.F. Besier, P.N. Smith, Statistical shape modelling reveals large and distinct subchondral bony differences in osteoarthritic knees, *J. Biomech.* 93 (2019) 177–184, doi:10.1016/j.jbiomech.2019.07.003.
- [22] P. Cerveri, A. Belfatto, A. Manzotti, Pair-wise vs group-wise registration in statistical shape model construction: representation of physiological and pathological variability of bony surface morphology, *Comput. Methods Biomech. Biomed. Eng.* 22 (2019) 772–787, doi:10.1080/10255842.2019.1592378.
- [23] A. Marzola, F. Buonamici, L. Guariento, L. Governi, Enhanced statistical shape model: a statistical-based tool to design custom orthopaedic devices, in: C. Rizzi, F. Campana, M. Bici, F. Gherardini, T. Ingrassia, P. Cicconi (Eds.), *Design Tools and Methods in Industrial Engineering II*. ADM 2021. Lecture Notes in Mechanical Engineering, Springer, Cham, 2022, pp. 27–38, doi:10.1007/978-3-030-91234-5_3.
- [24] M.A. Fuessinger, S. Schwarz, J. Neubauer, C.P. Cornelius, M. Gass, P. Poxleitner, R. Zimmerer, M.C. Metzger, S. Schlager, Virtual reconstruction of bilateral midfacial defects by using statistical shape modeling, *J. Cranio Maxillofac. Surg.* 47 (2019) 1054–1059, doi:10.1016/j.jcms.2019.03.027.
- [25] W. Semper-Hogg, M.A. Fuessinger, S. Schwarz, E. Ellis, C.P. Cornelius, F. Probst, M.C. Metzger, S. Schlager, Virtual reconstruction of midface defects using statistical shape models, *J. Cranio Maxillofac. Surg.* 45 (2017) 461–466, doi:10.1016/j.jcms.2016.12.020.
- [26] C.P. Klingenberg, Walking on Kendall's shape space: understanding shape spaces and their coordinate systems, *Evol. Biol.* 47 (2020) 334–352, doi:10.1007/s11692-020-09513-x.
- [27] F.L. Bookstein, Size and shape spaces for landmark data in two dimensions, *Stat. Sci.* 1 (1986), doi:10.1214/ss/1177013696.
- [28] I.T. Jolliffe, *Principal Component Analysis*, 2nd ed., Springer-Verlag, New York, 2002, doi:10.1007/b98835.
- [29] O. van Kaick, H. Zhang, G. Hamarneh, D. Cohen-Or, A survey on shape correspondence, *Comput. Graph. Forum* 30 (2011) 1681–1707, doi:10.1111/j.1467-8659.2011.01884.x.
- [30] T. Albrecht, M. Lüthi, T. Gerig, T. Vetter, Posterior shape models, *Med. Image Anal.* 17 (2013) 959–973, doi:10.1016/j.media.2013.05.010.
- [31] P.J. Besl, N.D. McKay, A method for registration of 3-D shapes, *IEEE Trans. Pattern Anal. Mach. Intell.* 14 (1992) 239–256, doi:10.1109/34.121791.
- [32] Y. Chen, G. Medioni, Object modeling by registration of multiple range images, *Image Vis. Comput.* 10 (1992) 145–155, doi:10.1016/0262-8856(92)90066-C.
- [33] A. Myronenko, Xubo Song, Point set registration: coherent point drift, *IEEE Trans. Pattern Anal. Mach. Intell.* 32 (2010) 2262–2275, doi:10.1109/TPAMI.2010.46.
- [34] F.M. Vos, P.W. de Bruin, J.G.M. Aubel, G.J. Streekstra, M. Maas, L.J. van Vliet, A.M. Vossepoel, A statistical shape model without using landmarks, in: *Proceedings of the 17th International Conference on Pattern Recognition*, 3, ICP 2004., IEEE, 2004, 2004, pp. 714–717, doi:10.1109/ICPR.2004.1334628.
- [35] A.D. Brett, C.J. Taylor, A method of automated landmark generation for automated 3D PDM construction, *Image Vis. Comput.* 18 (2000) 739–748, doi:10.1016/S0262-8856(99)00077-3.
- [36] A. Marzola, C. Robilotto, Y. Volpe, L. Governi, R. Furferi, Statistical shape model: comparison between ICP and CPD algorithms on medical applications, *Int. J. Interact. Des. Manuf. IJIDeM* 15 (2021) 85–89, doi:10.1007/s12008-020-00725-1.
- [37] H. Abdi, L.J. Williams, *Principal component analysis*, Wiley Interdiscip. Rev. Comput. Stat. 2 (2010) 433–459, doi:10.1002/wics.101.

- [38] G.H. Golub, C. Reinsch, Singular value decomposition and least squares solutions, *Numer. Math. Heidelb* 14 (1970) 403–420, doi:[10.1007/BF02163027](https://doi.org/10.1007/BF02163027).
- [39] S. Chilamkurthy, R. Ghosh, S. Tanamala, M. Biviji, N.G. Campeau, V.K. Venugopal, V. Mahajan, P. Rao, P. Warier, Development and Validation of Deep Learning Algorithms for Detection of Critical Findings in Head CT Scans, *Computer Vision and Pattern Recognition*. (2018), doi: 10.48550/arXiv.1803.05854. CQ500 Dataset, (n.d.). <http://headctstudy.qure.ai/dataset> (accessed December 5, 2022).
- [40] R.H. Davies, *Learning Shape: Optimal Models For Analysing Natural Variability*, University of Manchester, 2002.
- [41] M.A. Styner, K.T. Rajamani, L.P. Nolte, G. Zsemlye, G. Székely, C.J. Taylor, R.H. Davies, Evaluation of 3D correspondence methods for model building, in: 2003: pp. 63–75. doi:[10.1007/978-3-540-45087-0_6](https://doi.org/10.1007/978-3-540-45087-0_6).
- [42] S.T. Gollmer, T.M. Buzug, A method for quantitative evaluation of statistical shape models using morphometry, in: *Proceedings of the 2010 IEEE International Symposium on Biomedical Imaging: From Nano to Macro*, IEEE, 2010, pp. 448–451, doi:[10.1109/ISBI.2010.5490312](https://doi.org/10.1109/ISBI.2010.5490312).
- [43] R. Davies, C. Twining, C. Taylor, *Statistical Models of Shape: Optimisation and Evaluation*, Springer London, London, 2008, doi:[10.1007/978-1-84800-138-1](https://doi.org/10.1007/978-1-84800-138-1).
- [44] H. Lamecker, M. Seebass, H.C. Hege, P. Deuffhard, A 3D statistical shape model of the pelvic bone for segmentation, *Proc. SPIE 5370, Medical Imaging 2004: Image Processing* (2004), 1341, doi:[10.1117/12.534145](https://doi.org/10.1117/12.534145).
- [45] R.H. Davies, C.J. Twining, T.F. Cootes, C.J. Taylor, Building 3-D statistical shape models by direct optimization, *IEEE Trans. Med. Imaging* 29 (2010) 961–981, doi:[10.1109/TMI.2009.2035048](https://doi.org/10.1109/TMI.2009.2035048).
- [46] L. di Angelo, P. di Stefano, L. Governi, A. Marzola, Y. Volpe, Can MaWR-method for symmetry plane detection be generalized for complex panfacial fractures?, in: S. Gerbino, A. Lanzotti, M. Martorelli, R. Mirálbes Buil, C. Rizzi, L. Roucoules (Eds.) *Advances on Mechanics, Design Engineering and Manufacturing IV*. JCM 2022. *Lecture Notes in Mechanical Engineering*, Springer, Cham, 2023, pp. 148–158, doi:[10.1007/978-3-031-15928-2_13](https://doi.org/10.1007/978-3-031-15928-2_13).